PAPER

Characterization of the iron oxide phases formed during the synthesis of core–shell Fe_xO_y@C nanoparticles modified with Ag

To cite this article: D A Petrov *et al* 2020 *Nanotechnology* **31** 395703

IOP Publishing Nanotechnology

Nanotechnology **31** (2020) 395703 (12pp) https://doi.org/10.1088/1361-6528/ab9af2

Characterization of the iron oxide phases formed during the synthesis of core–shell Fe_xO_y@C nanoparticles modified with Ag

D A Petrov[1], C -R Lin[2], R D Ivantsov[1], S G Ovchinnikov[1,3], S M Zharkov[1,3], G Y Yurkin[1,3], D A Velikanov[1], Y V Knyazev[1,3], M S Molokeev[1,3], Y -T Tseng[2], E -S Lin[2], I S Edelman[1], A O Baskakov[4], S S Starchikov[4] and I S Lyubutin[4]

[1] Kirensky Institute of Physics, FRC, KSC, SB RAS, Krasnoyarsk 660036, Russia
[2] National Pingtung University, Pingtung City, Pingtung County 90003, Taiwan
[3] Siberian Federal University, Svobodny Av., 79, Krasnoyarsk 660041, Russia
[4] Shubnikov Institute of Crystallography of FSRC 'Crystallography and Photonics' RAS, Moscow 119333, Russia

E-mail: irbiz@iph.krasn.ru and crlinspin@gmail.com

Received 2 March 2020, revised 4 June 2020
Accepted for publication 9 June 2020
Published 7 July 2020

Abstract

Core–shell Fe_xO_y@C nanoparticles (NPs) modified with Ag were studied with x-ray diffraction, transmission electron microscopy, energy dispersive elemental mapping, Mössbauer spectroscopy, static magnetic measurements, and optical magnetic circular dichroism (MCD). Fe_xO_y@C NPs synthesized by the pyrolysis process of the mixture of $Fe(NO_3)_3 \cdot 9H_2O$ with oleylamine and oleic acid were added to a heated mixture of oleylamine and $AgNO_3$ in different concentrations. The final product was a mixture of iron oxide crystalline NPs in an amorphous carbon shell and Ag crystalline NPs. The iron oxide NPs were presented by two magnetic phases with extremely close crystal structures: Fe_3O_4 and γ-Fe_2O_3. Ag is shown to form crystalline NPs located very close to the iron oxide NPs. An assumption is made about the formation of hybrid Fe_xO_y@C-Ag NPs. Correlations were obtained between the Ag concentration in the fabricated samples, their magnetic properties and the MCD spectrum shape. Introducing Ag led to a approximately linear decrease of the NPs saturation magnetization depending upon the Ag concentration, it also resulted into the MCD spectrum shift to the lower light wave energies. MCD was also studied for the Fe_3O_4@C NPs synthesized earlier with the same one-step process using different heat treatment temperatures, and MCD spectra were compared for two series of NPs. A possible contribution of the surface plasmon excitation in Ag NPs to the MCD spectrum of the Fe_xO_y@C-Ag NPs is discussed.

Keywords: core–shell nanoparticles, iron oxides, carbon shell, Ag nanoparticles

(Some figures may appear in colour only in the online journal)

1. Introduction

Iron oxide nanoparticles (NPs), magnetite (Fe_3O_4) and maghemite (γ-Fe_2O_3), are very popular because of their specific magnetic properties and a wide range of practical applications. Magnetite has the inverse spinel structure of the space group *Fd*3*m*. The oxygen ions, O^{2-}, form a face-centered-cubic (*fcc*) lattice. The unite cell consisting of 32 O^{2-} ions contains eight Fe^{3+} and eight Fe^{2+} cations occupying octahedral positions (B sites), and eight Fe^{3+} cations in tetrahedral positions (A sites). Cations in the B and A sites form two magnetic sublattices with the oppositely directed magnetic moments, and

the total magnetic moment is determined by the B sublattice [1]. Heating of Fe_3O_4 transforms it into a more stable phase γ-Fe_2O_3. Maghemite, similar to magnetite, is a spinel with a cubic ($P4_132$) or tetragonal ($P4_12_12$) unit cell. Its unit cell is similar to the magnetite one, but contains only Fe^{3+} cations—16 in B, and 8 in A sites, while 1/6 of the octahedral positions remains unfilled with cations, which creates oxygen vacancies. As a result, both magnetite and maghemite are ferrimagnetic compounds with the magnetic ordering temperatures of the bulk samples ~550 °C and ~675 °C, respectively. Fe_3O_4 begins to turn into γ-Fe_2O_3 at fairly low temperatures, therefore magnetite NPs are often coated with a thin maghemite shell that was used for the synthesis of Fe_3O_4@γ-Fe_2O_3 core–shell NPs [2–8]. The size of such particles varies within 2–30 nm with the γ-Fe_2O_3 shell thickness of 1–5 nm. These NPs have, in some cases, a large magnetic moment (>60 emu g^{-1}). In work [8], it was proposed to use them as nano-heaters for *in vitro* magnetic hyperthermia.

To protect NPs from environmental damages and prevent their agglomeration, some authors use a carbon shell coating of NPs. Such Fe_3O_4@C NPs [9] and γ-Fe_2O_3@C NPs are used for making anodes for lithium-ion batteries [10, 11]. γ-Fe_2O_3@C nanorods can be used as lightweight microwave materials [12]. Fe_3O_4@C nanocomposite showed high specific capacitance with the stable cycling performance and can be used in an asymmetric supercapacitor [13]. In most cases, iron oxide-carbon core–shell NPs were prepared in two stages: the synthesis of the NPs core and then coatings them by the carbon shell. In [14], a one-step process of thermal decomposition was proposed in order to fabricate Fe_3O_4@C NPs. Strong dependence of the NPs core composition and properties on the processing temperature was revealed. The NPs synthesized at temperatures higher than 360 °C were covered by the amorphous carbon shell of about several nanometers in thickness. The Fe_3O_4 NPs appeared at temperatures of about 340 °C–350 °C and the pure Fe_3O_4 phase was created when the processing temperature increased to 380 °C. At higher temperatures, transformation of the magnetite core fragments into wüstite FeO was observed under the influence of carbon. As the amount of wüstite in the samples increased, the magnetization greatly decreased. Here we dwelled on the results of this work in detail since we used this technology for the one-step Fe_xO_y@C NPs fabrication.

Some authors use Fe_3O_4@C NPs decorated by Ag to expand the field of their application. Usually, Ag NPs of 10–30 nm in size are attached to larger Fe_3O_4@C NPs forming a non-continuous Ag shell. Such Fe_3O_4@C@Ag NPs could have antibacterial activity [15] due to Ag NPs. A high catalytic activity of these NPs [16–19] allows one to make nano-biosensors [20] and sensors for organic pollutants detection [19, 21, 22]. These NPs have a magnetic moment 25–50 emu g^{-1} that can be enough to provide a possibility of the NPs removal by means of a magnetic field and their re-use, or a possibility of manipulating the NPs motion for the application in drug delivery [23]. The magnetic properties both of the core and the whole NPs strongly depend on the synthesis conditions. Thus, they must be investigated for any specific method of their preparation.

In our recent paper [24], we studied the magnetic and magneto-optical properties of the Fe_3O_4 NPs modified with Ag and revealed noticeable changes in the magnetic and magneto-optical properties with the change of the relative concentration of the Fe_3O_4 and Ag constituents in the sample which were ascribed to the interfacial effects at the boundaries of the Fe_3O_4 and Ag NPs. Here, we extended the same approach to study a mixed system including iron oxide (Fe_xO_y)-carbon core–shell NPs with different x and y values and Ag NPs at the changing concentration. To fabricate Fe_3O_4@C NPs we used the one-step process of thermal decomposition [14]. In this connection, along with the widely used methods of x-ray diffraction, electron microscopy, and magnetometry, we applied, as in [24], spectroscopy of magnetic circular dichroism (MCD) that informs about the structure of excited electronic states of matter. Besides, the MCD spectra of magnetite and maghemite phases are quite different [25] which allows one to distinguish these two phases very well. This method was applied to study both the Fe_xO_y@C samples modified with Ag and analogous samples without Ag investigated earlier in [14].

2. Experimental

2.1. Synthesis procedure

Nanostructured samples containing a magnetic core—carbon shell (Fe_xO_y@C) NPs and Ag NPs were fabricated in the two-stage process. At the first stage, core–shell NPs were synthesized by pyrolysis using the approach described in [14]. 8 mmol $Fe(NO_3)_3$•$9H_2O$ was dissolved in a mixture solution of oleylamine $C_{18}H_{37}N$ (OLA) and oleic acid $C_{18}H_{34}O_2$ (OA), to be followed by several procedures for heating the solution: 140 °C for 0.5 h, 240 °C for 1 h and 370 °C for 1 h. The final reaction temperature 370 °C was chosen based on the results of [14] where the range of temperatures 350 °C–400 °C was used and wüstite phase formation was shown at higher temperatures. On the other hand, at lower temperatures the formation of carbon shell was not guaranteed. After cooling, the NPs were separated from the suspension by the magnetic field and several times washed with hexane and ethanol. Thus, Fe_xO_y magnetic particles coated by a carbon shell were formed, i.e. Fe_xO_y@C.

At the second stage, a mixture of a mmol of $AgNO_3$ and 8 ml of OLA was heated to 160 °C under stirring and addition of Fe_3O_4@C NPs to this solution. The reaction time was 0.5 h. The $AgNO_3$ concentration (a mmol) in the mixture varied in wide range (table 1). The atomic molar ratios of Ag/Fe in the samples, according to the components concentration in the mixture are presented in table 1.

It seemed interesting to compare some of the properties of NPs synthesized in this way with the properties of NPs presented in [14], especially since for the latter ones MCD had not been previously studied. We chose a series of NPs made in [14] at different temperatures and since this series had been made earlier we designated it as series 1, and the samples made in this work were designated as series 2. In the first series, the

Table 1. The atomic molar ratios Ag/Fe and mole number *a* of $AgNO_3$ used in the sample preparation.

Sample	atomic molar ratio Ag/Fe	mole number of $AgNO_3$ (*a* mmol)
1	0.00	0.00
2	0.01	0.05
3	0.02	0.12
4	0.03	0.25
5	0.06	0.47
6	0.06	0.50
7	0.12	0.95
8	0.13	1.00
9	0.25	2.00
10	0.35	2.80

samples differed in the heating temperature, and in the second series in silver concentration.

2.2. Methods of characterization

The powder diffraction data for Rietveld analysis were collected at room temperature with a Bruker D8 ADVANCE powder diffractometer (Cu-Kα radiation) and linear VANTEC detector. The step size of 2θ was 0.016°, and the counting time was 5 s per step. Rietveld refinement was performed by using TOPAS 4.2 [26].

The Mössbauer spectra of the samples were obtained on a MS-1104Em spectrometer in transmission geometry with a Co^{57} (Rh) radioactive source at 300 K. The processing was performed in two stages. At the first stage, possible nonequivalent iron positions in the samples were determined by calculating the probability distributions of magnetic hyperfine fields. In accordance with the results obtained, a preliminary model spectrum was formed. At the next stage, the model spectrum was fitted to the experimental one by varying the entire set of hyperfine parameters using the linear approximation of the least squares method.

The morphology, microstructure and local elemental composition of the NPs were investigated using transmission electron microscopy (TEM) using a JEM-2100 (JEOL Ltd.) microscope operating at the accelerating voltage of 200 kV. The microscope was equipped with an energy dispersive spectrometer (EDS), Oxford Instruments, which was used to control the elemental composition of the samples. Selected-area electron diffraction (SAED) was used to determine the structure of NPs.

Magnetization field dependences at room temperature and temperature dependencies of magnetization were recorded with the quantum design SQUID magnetometer for two cooling regimes—in the magnetic field of 0.1 T (FC) and without the magnetic field (ZFC).

To carry out the optical magnetic circular dichroism (MCD) measurements, transparent composite plates containing the NPs were prepared: the NPs powder was mixed with a dielectric transparent silicon-based glue ('Rayher' art. nr. 3 338 100 80 ml) in the weight proportion 0.5/100 and measures were taken to obtain homogeneous particle distribution in a matrix such as ultrasonic bath. The mixture was placed between two thin glass plates spaced by wires 0.15 mm in diameter and solidified. The low magnetic powder concentration allowed us to exclude the interaction between the NPs.

MCD was measured in the normal geometry: the magnetic vector and light beam were directed normal to the plate plane. The modulation of the light wave polarization state from the right-hand to the left-hand circular polarization relatively to the magnetic field direction was used for the MCD measurements. The MCD value was measured as the difference between the sample optical density, D, for the right (+) and left (-) polarized light waves ($\Delta D = D_{+} - D_{-}$) in the spectral range of 1.2–3.9 eV in a magnetic field of 1.3 T at the temperature of 300 K. The measurement accuracy was about 10^{-4}, and the spectral resolution was 20–50 cm^{-1} depending on the wavelength.

3. Results and discussion

3.1. X-ray diffraction analysis

Rietveld analysis was performed for samples 9 and 10 which differed in the Ag/Fe ratio. All peaks were indexed by two cubic phases with the parameters close to Fe_3O_4 and Ag (figure 1). The XRD analysis does not always allow distinguishing between magnetite, Fe_3O_4, and maghemite, γ-Fe_2O_3, phases, because of their close crystal structures. Moreover, several modifications of the maghemite crystal structure are known [27]. Two of them are usually reported: the cubic structure of the $P4_132$ space group (PDF card # 00–039-1346) with $a = 8.3515(22)$ Å and the tetragonal structure of the $P4_12_12$ space group with $c/a = 3$. The first one was shown in [27] to be more stable than all other modifications. The interplanar spacing for this symmetry is very close to that for Fe_3O_4. Taking into account the broadening of reflections associated with the nanoscale particles, the coincidence can be considered almost complete. Thus, the Fe_3O_4 and Ag crystal structures were taken as the starting model for Rietveld refinement. The refinement was stable and gave low *R*-factors (table 2).

In table 3, the parameters of the most intense XRD peaks for the cubic γ-Fe_2O_3 and Fe_3O_4 phases obtained from PDF Cards # 00–039-1346 and # 04–005-4319 are presented. All intense positions are seen to be the same for both phases. Two weak peaks at small angles (marked with arrows in figure 1.) are the exception: they are observed only for maghemite. Thus, most of the peaks in the XRD patterns can be attributed both to Fe_3O_4 and to γ-Fe_2O_3, however, the peaks at small angles indicate the presence of a certain amount of the cubic γ-Fe_2O_3 phase in the samples.

The difference between the shapes of patterns is mainly due to the presence of an amorphous phase in sample 9 as it will be seen from the Mössbauer data.

3.2. Transmission electron microscopy analysis

In figure 2, the TEM images of three samples of series 2—one containing no Ag (figure 2(a)) and two with high Ag content (figures 2(d) and (f)) are presented. Ellipses, quadrangles and

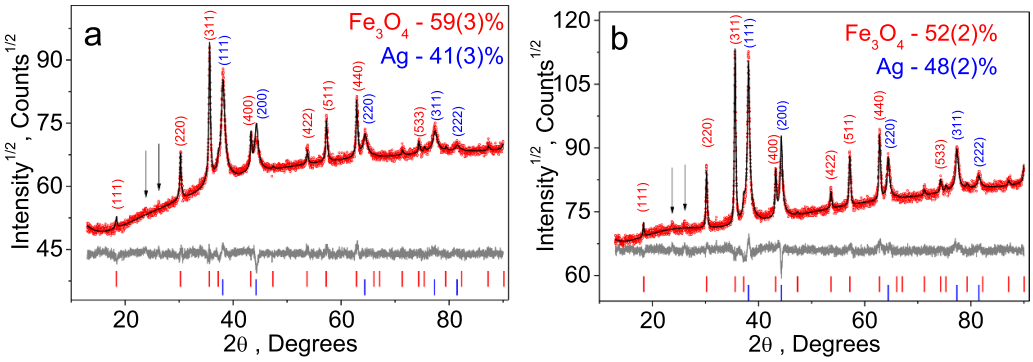

Figure 1. XRD diffraction patterns and difference Rietveld plots for samples 9 (a) and 10 (b).

Table 2. Main crystallographic parameters of processing and refinement for samples 9 and 10.

Sample	Phase	Weight (%)	Space group	Cell parameters (Å), Cell volume (Å^3)	R_{wp}, R_p (%), χ^2	R_B (%)
9	Fe_3O_4	59(3)	$Fd-3\,m$	$a = 8.3571(9)$, $V = 583.7(2)$	2.12, 1.60, 1.37	0.81
	Ag	41(3)	$Fm-3\,m$	$a = 4.0891(5)$, $V = 68.37(3)$		0.90
10	Fe_3O_4	52(2)	$Fd-3\,m$	$a = 8.364(1)$, $V = 585.2(3)$	1.92, 1.43, 1.48	1.81
	Ag	48(2)	$Fm-3\,m$	$a = 4.0875(9)$, $V = 68.29(5)$		0.51

Table 3. Characteristics of some XRD peaks for γ-Fe_2O_3 and Fe_3O_4, according to the database ICDD PDF 4 + [28], d is the interplanar spacing.

γ-Fe_2O_3, PDF Card # 00–039-1346				Fe_3O_4, PDF Card # 04–005-4319			
2θ	d (Å)	I	h k l	2θ	d (Å)	I	h k l
14.9575	5.918	5	110				
18.3839	4.822	4	111	18.2871	4.847	8	111
23.7711	3.740	5	210	–	–	–	–
26.1025	3.411	5	211	–	–	–	–
30.2406	2.953	35	220	30.0804	2.968	29	220
35.6302	2.517	100	311	35.4305	2.531	100	311
–	–	–	–	37.0619	2.424	8	222
43.2835	2.089	16	400	43.0594	2.099	21	400
53.7325	1.704	10	422	53.4181	1.714	9	422
57.2714	1.607	24	511	56.9436	1.616	28	511
62.9250	1.476	34	440	62.5295	1.484	38	440
74.4707	1.273	5	533	73.9716	1.280	7	533

hexagons with rounded corners with the characteristic sizes of 20–40 nm are the main types of the NPs observed. Besides, octagons and the irregular shaped NPs are also visible. Larger particles up to 80–150 nm are also observed. At the same time, smaller rounded completely opaque to electrons NPs with a size of 5–15 nm (sometimes larger) are observed in the samples containing Ag, figures 2(d)–(f). It seems reasonable to refer these objects to Ag NPs. The carbon shell of 1–3 nm in thickness can be seen only in the HRTEM images, figures 2(b) and (e). The shell is significantly thinner compared to the carbon shell thickness in the samples of series 1 synthesized at higher temperatures, as it is shown, for example, in the HRTM image of the sample synthesized at 395 °C, figure 2(c).

The EDS elemental mapping presented in figure 3 for sample 10 together with the STEM image of the same fragment confirmed the assumption that the dark spherical spots are silver NPs: here, the regions containing iron (red colored) and oxygen (green colored) correspond to iron oxide, and smaller spherical particles (blue colored) contain silver.

As seen from figures 2 and 3, the Ag NPs are located separately from the larger iron oxide NPs, but very close to them, possibly, attached to them. Similar pictures were observed in several works devoted to the iron oxide–Ag nanostructures [29–31]. Having in mind the idea to create new nanostructures by mixing noble metals and magnetic NPs for future applications, the authors of these works carried out two-stage synthesis of hybrid NPs iron oxide–Ag. So, for example, the authors of [29] added $AgNO_3$ solution to the α-Fe_2O_3 NPs which had been obtained by the reduction of Fe(III) chloride hexahydrate with sodium borohydride $NaBH_4$ and stabilized using polyvinylpyrrolidone (PVP) at constant concentration. According to [29], the ready-made α-Fe_2O_3 NPs can offer nucleation sites for forming Ag NPs through heterogeneous nucleation. Ag dissolution inside the iron oxide NPs cannot

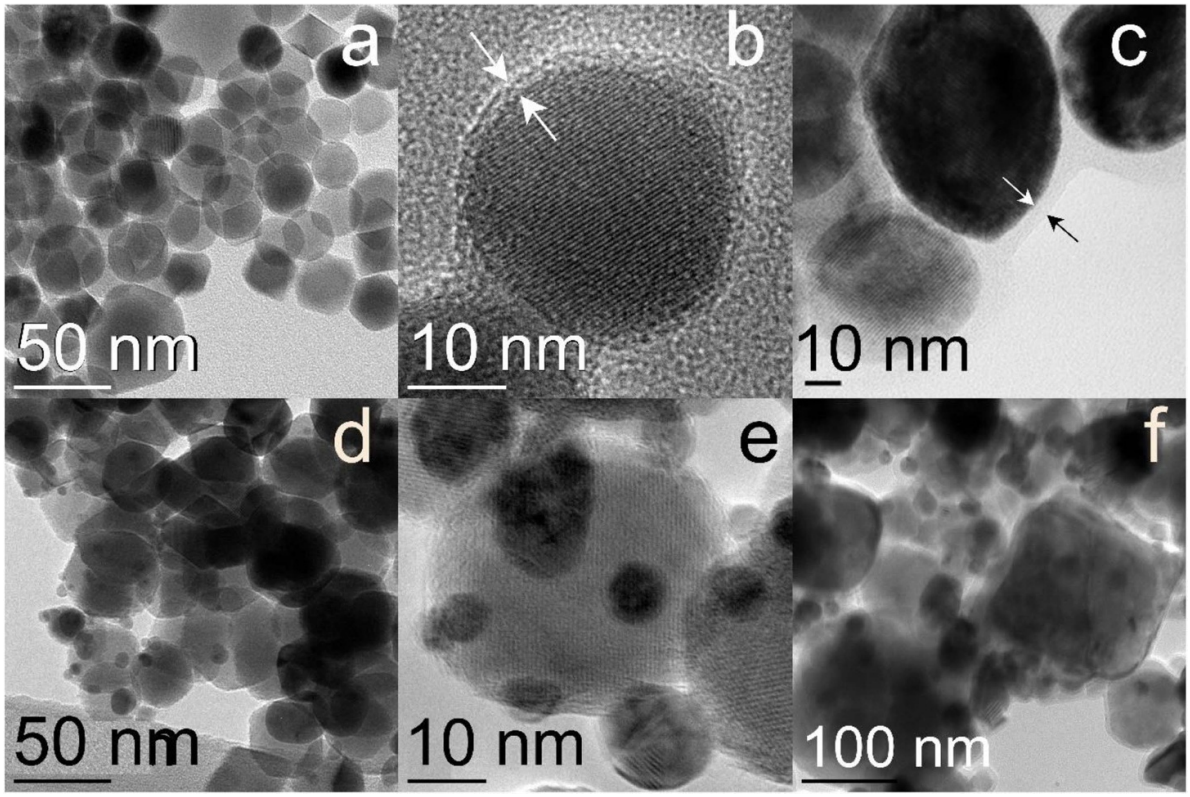

Figure 2. TEM (a, d) and HRTEM (b, e) images of the series 2 samples 1 (a, b) and 9 (d, e); the HRTEM image (c) of series 1 sample fabricated at 395 °C; TEM image (f) of the series 2 sample 10.

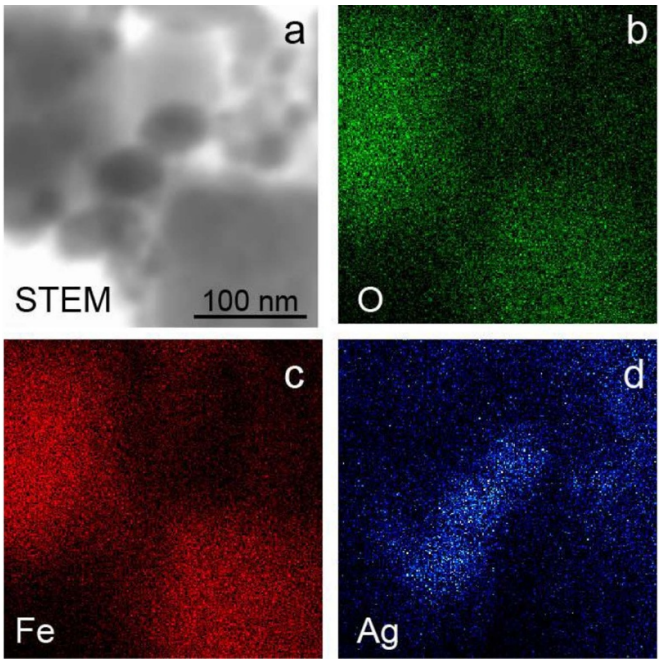

Figure 3. STEM image (a), and corresponding EDS elemental mapping images of O (b), Fe (c) and Ag (d) of sample 10. The scale is the same for all images.

occur since, generally, these elements are immiscible. For this scenario to be realized, the energy barrier for the Ag NPs nucleation from the $AgNO_3$ solution at the surface of the iron oxide NPs should be lower than that for the nucleation of individual Ag NPs. Based on the electrochemical analysis, the authors of [29] came to a conclusion that the formation of the discussed nanostructures was favored by the factors such as compensation charges generated by Ag and α-Fe_2O_3 NPs, which are derived from the structure type and the active sites of these entities. The principal similarity of the synthesis process used in this work with that used in the cited papers suggests that the proximity of the NPs observed in the electron microscope could correspond to the hybrid Fe_xO_y@C-Ag NPs. However, this issue needs a deeper study.

Analyzing the TEM images of the iron oxide NPs in the samples of series 2 and a possible connection of the NPs shape with a specific oxide phase, we can turn to the work of Morales *et al* [32] who reported that Fe_3O_4 NPs of 35 nm in size had quadrangle shape, while smaller γ-Fe_2O_3 NPs were ellipsoidal. Small Fe_3O_4 NPs (14 nm) were presented both by ellipsoidal and quadrangle shapes. Figures 4(a)–(c) present the size distribution of the particles of three main different shapes for samples 1, 7 and 9. The linear size of each particle was determined as the average value between its longitudinal and transverse linear dimensions. Since for further analysis it is necessary to evaluate the relative volume concentrations of the particles of various shapes, we assumed that they are three-dimensional with a thickness equal to the linear size in the plane. The volume distribution of the NPs obtained in this way is shown for the same samples 1, 7, 9 in figures 4(d)–(f). It can be seen that the distribution bar-graphs (histograms) are sharply different for these samples. The narrow distribution with the maxima in the size range of

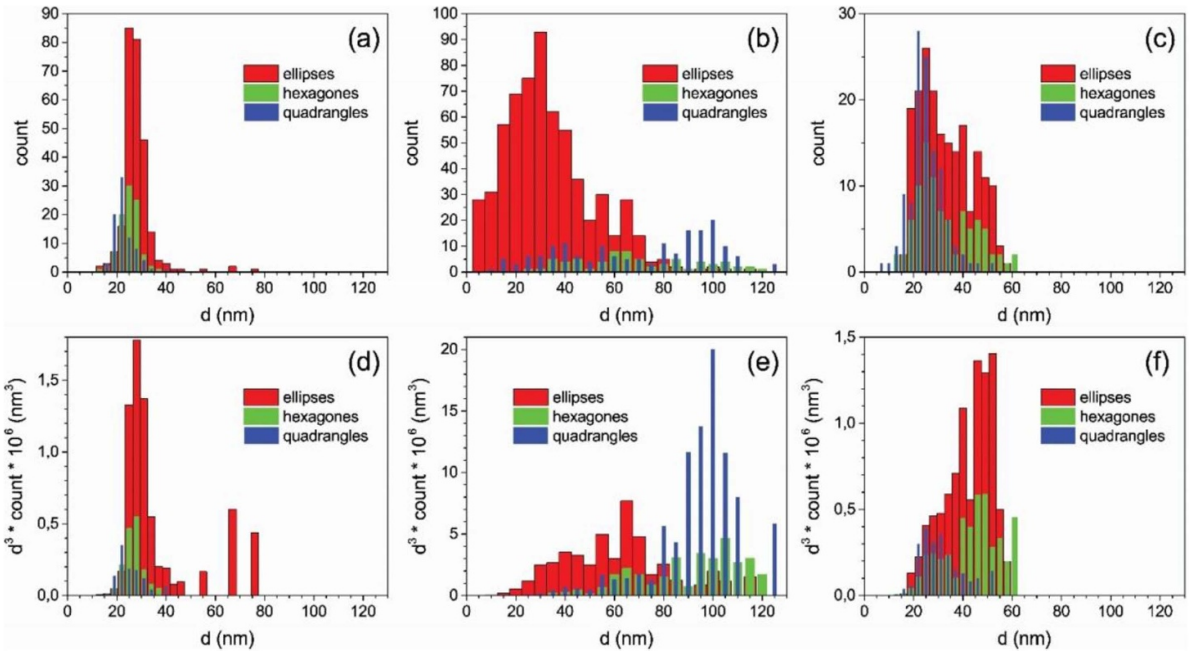

Figure 4. Particle size distribution (a, b, c) and volume occupied by these particles (d, e, f) for samples 1, 7, 9, respectively.

∼20–25 nm for the particles of different shapes is characteristic of sample 1. Moreover, the volume distribution graphs practically correspond to the size distribution ones with insignificant deviations in the region of the larger particles. Similar but wider size (figure 4(c)) and volume (figure 4(f)) distribution graphs are observed for sample 9, the graphs being symmetrical for the quadrangles and asymmetric for ellipses. For the NPs of the hexagonal shape, two-mode distribution graphs with the maxima at ∼25 and ∼47 nm are observed. A quite different situation is observed for sample 7—wide distribution graphs for the NPs of various shapes are characterized by far separated maxima for the ellipses (∼30 nm) and quadrangles (∼100 nm). Note the low quantity of hexagons in this sample and their random size distribution. According to Morales [32], we assume that the quadrangle particles could be considered to be Fe_3O_4. As the shape of the NPs approaches an ellipse, the situation becomes more complicated: the particles can consist both of magnetite and maghemite, as well as of their mixture. Thus, the question of relating the shape of the particles to a specific compound does not have a clear answer. However, in some cases, as will be shown below, there is a good agreement between the data of the particle shape analysis and the phase distribution of iron oxide in accordance with the Mössbauer effect.

The SAED patterns obtained from the Ag rich areas of the samples consisted of the distinct reflexes of fcc-Ag (PDF Card—Ag (*Fm*–3 *m*)—00-004-0783). In addition, in sample 10 containing a higher concentration of Ag, the formation of a phase based on Ag-Fe-O, for example $AgFeO_2$ (α-phase) was possible (PDF 4 + Card # 00–021-1081).

As concerns the iron oxide phases, the SAED patterns contain the same set of reflexes for all samples, analogously to the same set of peaks in the XRD patterns. In sample 9, along with the main reflexes there are also weak reflexes that could be associated with the γ-Fe_2O_3 phase like in the case of the weak peaks observed in XRD. So, SAED does not allow unambiguous distinguishing between magnetite and maghemite. Mössbauer spectroscopy is one of the most suitable methods for this aim, and it is described in the next paragraph.

3.3. Mössbauer spectroscopy

In order to more accurately determine the iron oxide phases in the samples, Fe^{57}-Mössbauer spectra were recorded and analyzed for some samples (figure 5). The results of the spectra processing are collected in table 4. The isomer shift (IS) characterizes the kind of local oxygen environment of iron (tetrahedral or octahedral), as well as the charge state of Fe ions. In the tetrahedral environment, the value of IS is lower than in the octahedral sites with the same charge state of iron due to the higher electron density on the Fe nuclei. A characteristic feature of magnetite is the presence of intermediate charge state $Fe^{2.5+}$ in octahedral sites (IS ∼ 0.5–0.7 mm s^{-1}) at room temperature, which is explained by the existence of fast electronic exchange between Fe^{2+} and Fe^{3+} ions. In the spectra obtained, the intensity of the Mössbauer lines characteristic of such a state of Fe increases from sample 9 (total absence of magnetite) to sample 7 (∼70% of the relative magnetite content). For these two samples, the phase composition of the studied NPs, estimated by the Mössbauer effect, is in good agreement with the estimation of the phase distribution based on the analysis of the particle shape, figures 4(e) and (f).

The hyperfine parameters presented in table 4 show that all the samples, with the exception of sample 9, contain magnetite NPs in different concentrations [33]. The highest fraction of magnetite is observed in sample 7. Maghemite NPs are observed in all samples. Sample 9 contains no magnetite; the main phase here is maghemite.

Table 4. Room-temperature Mössbauer parameters of the samples with different Ag content. IS is the isomer shift relative to α-Fe, H_{hf} is the magnetic hyperfine field at Fe nuclei, QS is the quadruple splitting, W is the width of the Mössbauer line at half-height, *A* is the relative occupancy of the position (VI—octahedral and IV—tetrahedral), S is a sextet, D is a doublet, Sg is a singlet.

Sample		IS, ±0.005 mm s^{-1}	H_{hf}, ±0.5 T	QS, ±0.02 mm s^{-1}	W, ±0.03 mm s^{-1}	*A*, ±0.03 o.e.	Position/Phase	
1	S2	0.339	503	0	0.42	0.23	Fe^{3+}-VI	γ-Fe_2O_3
	S1	0.304	487	0	0.41	0.24	Fe^{3+}-IV	Fe_3O_4
	S3	0.612	455	0.015	0.40	0.28	$Fe^{2.5+}$	
	D	0.393		0.677	0.58	0.05	superparamagnetic Fe	
	Sg	0.355			15.8	0.21	x-ray amorphous Fe	
3	S1	0.434	501	0	0.36	0.19	Fe^{3+}-VI	γ-Fe_2O_3
	S2	0.228	500	0.00	0.29	0.17	Fe^{3+}-IV	
	S3	0.333	482	−0.10	0.34	0.21	Fe^{3+}-IV	Fe_3O_4 defective
	S4	0.727	424	0	0.44	0.12	$Fe^{2.5+}$	
	D	0.316		0.76	0.64	0.03	superparamagnetic Fe	
	Sg	0.464			23.2	0.28	x-ray amorphous Fe	
7	S1	0.293	492	−0.03	0.31	0.26	Fe^{3+}	γ-Fe_2O_3
	S2	0.341	507	−0.01	0.36	0.35	Fe^{3+}-IV	Fe_3O_4
	S3	0.666	461	0.05	0.24	0.35	$Fe^{2.5+}$	
	D	0.393		0.76	0.58	0.04	superparamagnetic Fe	
9	S1	0.333	504	0	0.46	0.42	Fe^{3+}-VI	γ-Fe_2O_3
	S2	0.322	489	0	0.48	0.31	Fe^{3+}-IV	
	Sg	0.899			14.5	0.26	x-ray amorphous Fe	
10	S1	0.228	496	−0.10	0.34	0.18	Fe^{3+}-IV	γ-Fe_2O_3
	S2	0.324	511	0.02	0.40	0.26	Fe^{3+}-VI	
	S3	0.400	497	0	0.38	0.27	Fe^{3+}-VI	Fe_3O_4
	S4	0.564	450	0	0.43	0.28	$Fe^{2.5+}$	

In sample 1, one can note the presence of a paramagnetic doublet, which may be due to the superparamagnetic state of a part of the NPs. However, the appearance of β-Fe_2O_3, which has similar parameters with the paramagnetic doublet observed in this case, cannot be excluded [34].

A comparison of the Mössbauer spectroscopy data with the TEM images of the NPs confirms the assumption advanced above that the elliptical shape NPs are mainly the maghemite phase, and the faceted NPs can be attributed to the magnetite phase. The formation of particles of a more complex composition cannot be ruled out, for example, core–shell Fe_3O_4@γ-Fe_2O_3@C particles or coexistence of both phase grains inside the carbon shell. The first one is more probable since the appearance of γ-Fe_2O_3 is due to the oxidation of the Fe_3O_4 NPs surface, or full-length oxidation of small Fe_3O_4 NPs. Here, 23 molar percent of maghemite was detected with the Mössbauer data already in sample 1 after the first stage of sample synthesis. At the second stage of the synthesis, when Fe_3O_4@C NPs were introduced into $AgNO_3$ with OLA, the amount of γ-Fe_2O_3 phase increased non-monotonously. Apart from the two oxide phases described above, amorphous iron is detected in some samples and an insignificant amount of NPs is superparamagnetic at room temperature.

3.4. Magnetization measurements

In figure 6(a), magnetization curves *M*(*H*) are shown for samples 1, 9, 10. For other samples the magnetization curves are similar in shape. Moreover, the measured magnetization value was converted to the mass of the magnetic phase which was calculated taking into account the same amount of $Fe(NO_3)_3$•$9H_2O$, OLA, and OA in all samples and the corresponding mass of $AgNO_3$ used in the synthesis process. *M*(*H*) curves for all samples demonstrate hysteresis loops with the saturation field near 0.3 T and coercive field (H_c) varying from 5 to 19 mT. The *M*(*H*) curve for sample 1 of series 2 totally coincides with that for the 1st series sample prepared at 380 °C as it is presented in [14]. In both cases the saturation magnetization (M_s) is very close to the value of M_s = 67 emu g^{-1} observed in the bulk magnetite [35]. Figure 6(b) demonstrates the H_c and M_s dependencies on the Ag/Fe ratio. At low Ag concentrations, M_s fluctuates randomly between 68 and 57 emu g^{-1}. But there is a trend to the M_s decrease with the Ag concentration increase. This tendency turns into a pattern at higher silver concentrations. This phenomenon can be partially attributed to an increase in the content of the γ-Fe_2O_3 phase with a lower M_s value in the samples. However, the change in the amount of this phase in the samples does not strictly follow the increase in the Ag concentration. This is especially evident in samples 9 and 10. The decrease in the magnetization in nanostructures containing Fe_3O_4 and Ag NPs was noted previously, in particular, in [36] where the M_s decrease was associated with the formation of magnetically dead layers at the boundaries between Fe_3O_4 and Ag. The same mechanism can take place in our case. This correlates with the assumption made above about the formation of hybrid Fe_3O_4@C-Ag NPs in the studied samples.

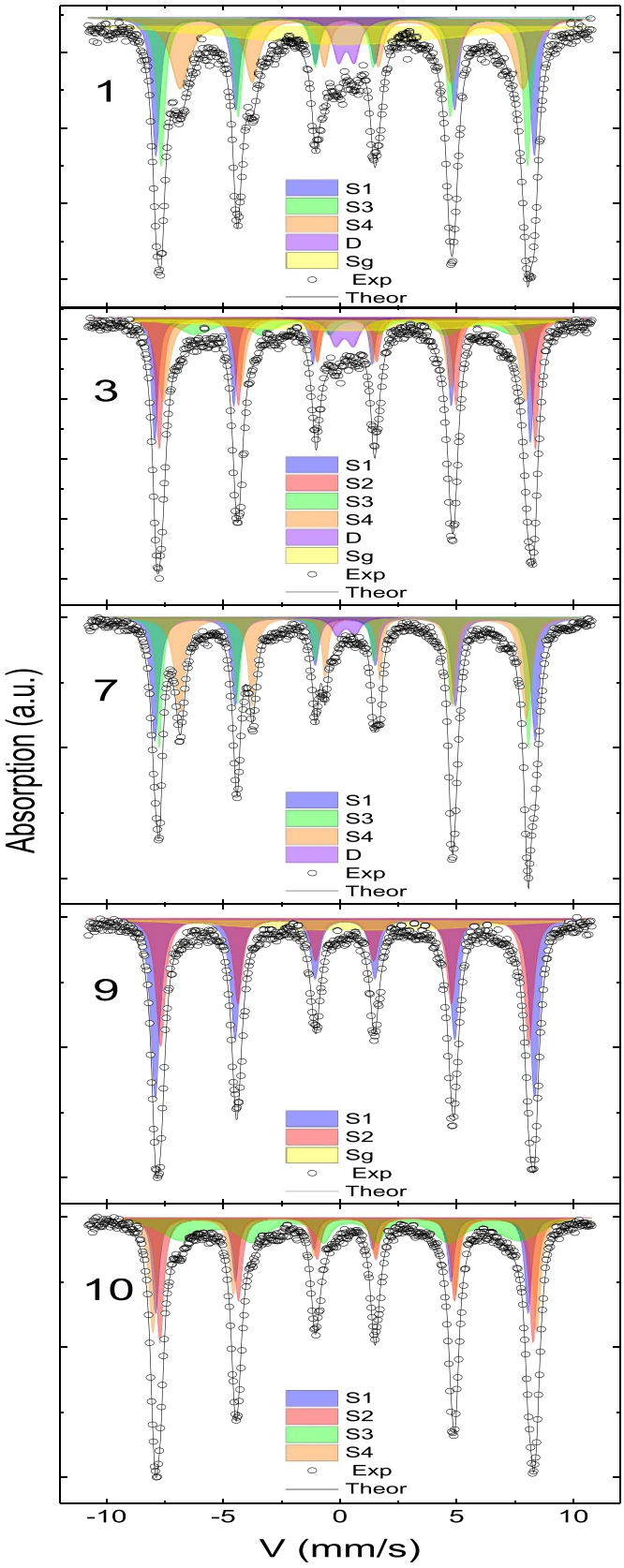

Figure 5. Room-temperature Mössbauer spectra of samples 1, 3, 7, 9, and 10. Partial spectra are shown as shaded areas: S1–S2 are sextets for Fe^{3+}-VI, Fe^{3+}-IV in γ-Fe_2O_3, S3–S4 are sextets for Fe^{3+}-IV, and $Fe^{2.5+}$ in Fe_3O_4, respectively, D is a doublet of superparamagnetic Fe, and Sg is a singlet of x-ray amorphous Fe.

The behavior of H_c demonstrates no definite tendency and changes non-monotonously in the limits of 10–17 mT with one exception for the ratio Ag/Fe = 0.25 (sample 9), when only the γ-Fe_2O_3 NPs are in the sample, according to the Mössbauer data (table 3).

The temperature dependences of the sample magnetization M(T) recorded in the field cooling (FC) and zero field cooling (ZFC) regimes are shown in figure 7 for samples 1 and 9. In sample 1, the ZFC curve includes two features. The feature near 120 K is close to the Verwey transition temperature T_V, which is about 123 K in bulk magnetite. The Verwey-type anomaly is a characteristic of magnetite, and its observation confirms the formation of magnetite NPs under these conditions of synthesis [14].

Similar ZFC curves were observed for other samples, except for sample 9. As it is seen from the Mössbauer data, sample 9 consists only of the γ-Fe_2O_3 phase without Fe_3O_4, therefore the thermomagnetic curves for this sample are associated with maghemite. The contribution of this phase is seen well for all other samples.

3.5. Magnetic circular dichroism measurements

In figure 8(a), the MCD spectra are shown recorded for the Fe_3O_4@C NPs of series 1 synthesized at temperatures from 360 to 400 °C by a continuous reaction involving a one-step thermal decomposition process. The structural and magnetic properties of these NPs were described in [14] as it was mentioned above. The spectra of all these samples demonstrate the same shape very similar to the magnetite, Fe_3O_4, MCD spectrum shape known in literature [37–40].

The non-monotonous change of the amplitude of the main spectral maxima corresponds to the change of the saturation magnetization of these samples presented in [14]: the amplitude increases with the increasing synthesis temperature (T_s), reaches the maximal value for the sample synthesized at T_s = 385 °C, and then decreases to almost zero. An analogous change in the magnetization value was associated in [14] with the reduction of magnetite Fe_3O_4 to wüstite $Fe_{1-x}O$ with the increasing synthesis temperature. Wüstite is antiferromagnetic with the Neel temperature of about 190 K, at higher temperatures it becomes paramagnetic. Thus, the behavior of the MCD spectra correlate well with the dynamics of thermal reduction of iron oxide from Fe_3O_4 to FeO under the influence of carbon in the carbon-encapsulated Fe_xO_y@C NPs.

The MCD spectra of the samples of series 2 are characterized by two maxima—positive and negative—similar to the samples of series 1. Several examples are shown in figure 8(b). For easy comparison of the spectra shape, we normalized the MCD value taking the amplitude of the high-energy MCD maximum of each sample as a unit. It is seen that at an increase of the Ag content in the samples, the overall form of the spectra varies little: wide positive and negative maxima remain prevailing in the spectra for all samples, except for sample 9. The intensities of the maxima change similarly to the changes in magnetization (figure 6(b)). This is not surprising since MCD is a linear function of the magnetization of the sample (recall that relative, rather than absolute, MCD values are shown in

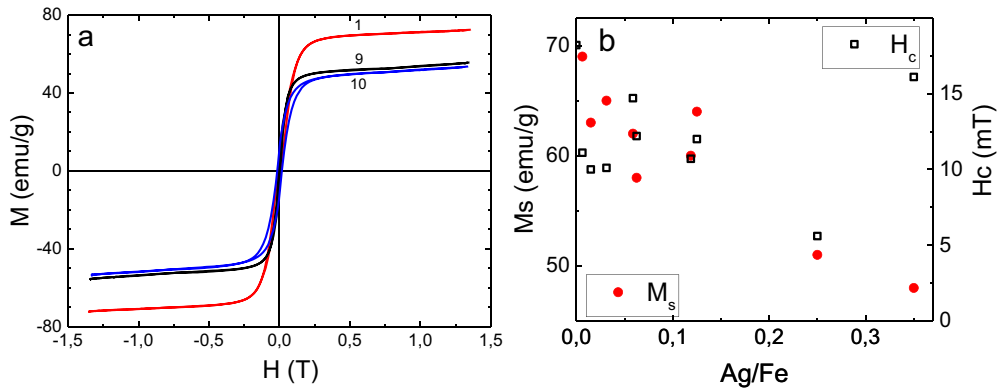

Figure 6. (a) Hysteresis loops for samples 1, 9, and 10. (b) the coercive field H_c (squares) and magnetization saturation M_s (circles) dependencies on the atomic molar ratio Ag/Fe.

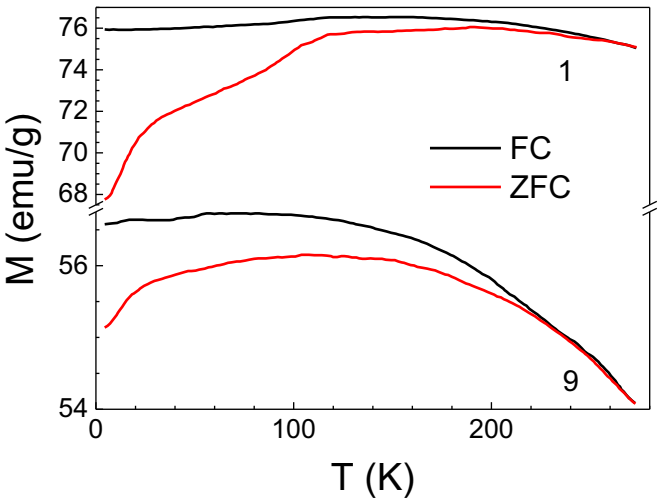

Figure 7. Temperature dependences of magnetization for samples 1 and 9 in the FC and ZFC regimes in the applied field of $H = 0.1$ T.

figure 8(b)). The maximum gravity centers shift noticeably to the lower energies, the higher the silver content in the samples. Only for sample 9, the MCD spectrum changes principally with respect to the rest of the samples, it is very close to the MCD spectrum of γ-Fe_2O_3 NPs presented in literature [25]. This observation corresponds to the Mössbauer spectrum analysis which shows the presence only of the γ-Fe_2O_3 phase in this sample (sample 9 in table 3). The γ-Fe_2O_3 contribution can be seen for all samples as some distortion of the spectral line near the MCD sign change. Such a distortion can be seen in the spectrum of series 1 sample synthesized at $T_s = 370$ °C (figure 8(a)). To understand the origin of the shift of the MCD maxima gravity centers to lower energies with an increase of the Ag content in the samples, we address the results of [39] where three bands were considered determining the main features in the MCD spectrum of the Fe_3O_4 thin film: the occupied t_2 band on the tetrahedral sublattice and partly occupied t_{2g} and unoccupied e.g. bands on the octahedral sublattice (figure 3 in [39]). Following [39], the intense positive maximum near 2 eV can be attributed to the electron transition from the occupied part of the t_{2g} band to the unoccupied higher *e.g.* band, while the negative maximum near 3 eV should be ascribed to the transition from the occupied t_2 band to the unoccupied part of the t_{2g} band.

The gradual shift of the maximum gravity centers with the increase of the Ag concentration is very similar to the shift of the analogous maxima in [39] with the increasing temperature above the Verwey temperature, i.e. with a sharp increase in the conductivity of the sample. Here, the proximity of Fe_3O_4 and Ag NPs can provide a monotonic change of the electron transfer between Fe_3O_4 and Ag because of the difference in the Fermi levels in these substances. The change of the free electrons density can cause an increase of the energies of the occupied and partly occupied bands and decrease of the energy of the interband electron transitions. The increase of the Ag content in the samples leads to the growth of the number of hybrid NPs and, as a consequence, to the growing energy shift of the MCD maxima. Therefore, one can suppose an effect of the Ag close neighboring in the Fe_3O_4 NPs electronic structure.

A question arises about the possibility to observe the surface plasmon resonance in Ag NPs because, according to the literature data, it should be excited near $E = 2.7$–2.8 eV [41] and the strong MCD peak associated with iron oxide phases is observed in this spectral interval, too. A contribution of the Ag NPs plasmon can be estimated from the comparison of the optical absorption spectra of the samples with Ag and without Ag.

Figure 9(a) shows the parts of the optical density spectra for sample 1 (without Ag) and sample 5 (with Ag). There are deviations of these curves from the fundamental absorption band which are more noticeable for sample 5. Such deviations are usually associated with the contributions of various types of weak electron transitions into the absorption. To identify the characteristics of such transitions, it is customary to represent such sections in the form of a sum of Gaussian contours. In our case, to describe the shape of the difference curve ΔD for sample 1, one Gaussian with a maximum of 3.4 eV is sufficient (figure 9(b)). At this energy, a negative maximum of MCD is observed, which should be associated with the electronic transition in iron oxide. For sample 5, the best fit was obtained, taking into account three contours with the centers of gravity 2.1, 2.7 and 3.2 eV. The last one can be associated with the electron transition in iron oxide as its energy coincides with the negative maximum in the MCD. The maximum

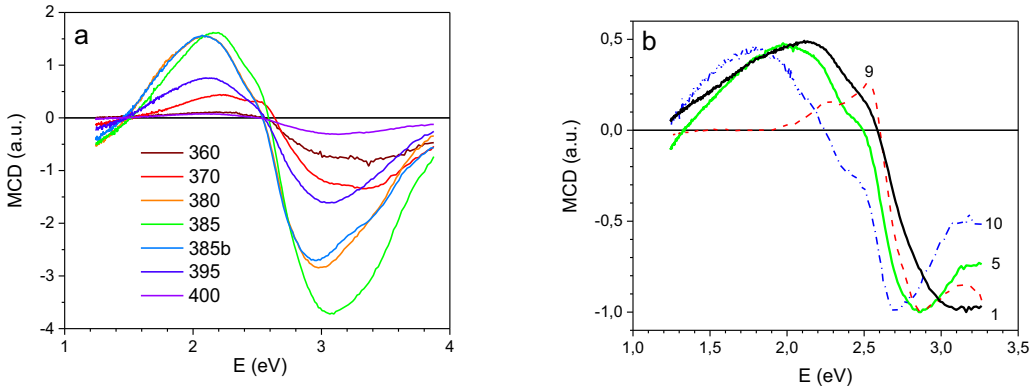

Figure 8. Room temperature MCD spectra (in an applied magnetic field of $H = 1.3$ T) for the Fe_3O_4@C NPs of series 1 synthesized at different temperatures (a) and for samples 1, 5, 9, 10 of the series 2 of Fe_xO_y@C NPs modified with Ag at different Ag concentrations (b).

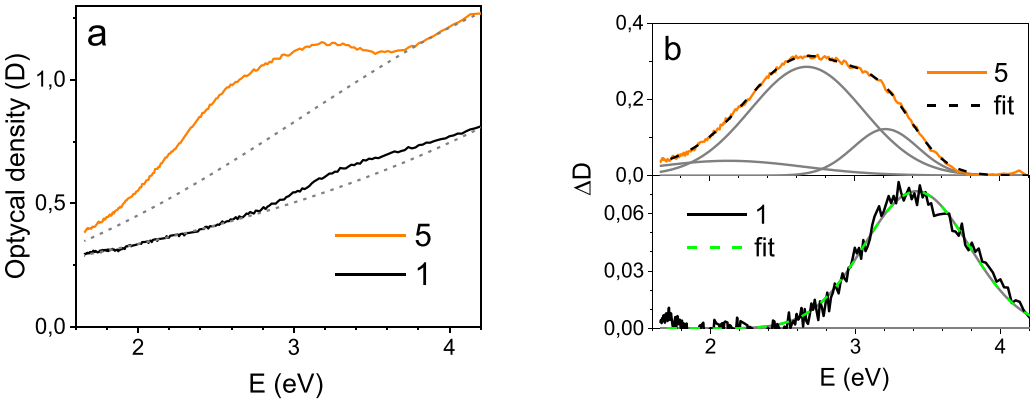

Figure 9. (a) Parts of the optical density (D) spectra for samples 1 and 5 of series 2 (solid lines). The dashed lines correspond to the fundamental edge obtained by the approximation of D curve in the interval 1.6–4.2 eV. (b) The differences (ΔD) between the experimental and approximated optical density spectra, and ΔD fitting (dashed lines) by the Gauss contours (gray lines) for samples 1 and 5.

at 2.1 eV also corresponds to the positive MCD maximum in Fe_3O_4. The strong maximum at 2.7 eV appeared only for the samples containing Ag. This energy approximately corresponds to the energy of the surface plasmon resonance (SPR) observed by many authors in spherical Ag NPs (e.g. [42],). Generally, the SPR energy depends on the NPs shape, size, filling fraction in the matrix, and matrix dielectric constant. For the spherical NPs, an increase in the last three parameters leads to a shift in the SPR maximum to lower energies. In the region of the SPR excitation in the Ag NPs, a MCD signal was detected [43–46] in the form of the s-shape curve with the higher energy positive peak and the lower energy negative peak and intersection with the energy axis in the point of the SPR maximum. The negative peak practically coincides with the negative MCD peak of iron oxides. Thus, the peak seen in figure 8(b) in the region of 2.7–3.2 eV depending on the Ag concentration can be considered as a sum of two very close situated peaks—MCD in iron oxide NPs and MCD due to SPR in Ag NPs. As the Ag concentration increases, the intensity of the peak associated with SPR in the Ag NPs increases and the total peak shifts to the lower energies as it is observed in experiment. Thus, several mechanisms may be responsible for the shift of the MCD spectrum. Additional experiments to ascertain the nature of such a shift are in progress.

4. Conclusion

Morphology, structure, magnetic phase composition, magnetization dependences on temperature and an external magnetic field, Mössbauer spectra and optical magnetic circular dichroism were studied in the core–shell iron oxide–carbon, Fe_xO_y@C, NPs modified with Ag in comparison with the Fe_xO_y@C NPs investigated earlier [14] by several authors of the team. The Fe_xO_y@C NPs were synthesized by pyrolysis of $Fe(NO_3)_3$•$9H_2O$, oleylamin (OLA), and oleic acid (OA) under the conditions based on the previously obtained results. In particular, the chosen pyrolysis temperature, 370 C, provided the formation of ferrimagnetic phases of iron oxide excluding the appearance of antiferromagnetic wüstite phase FeO.

The XRD data analysis revealed two crystalline phases in all samples synthesized at 370 C: (i) The iron oxide nanocrystals with the parameters that can be attributed both to magnetite Fe_3O_4 and maghemite γ-Fe_2O_3 as these crystals are known to be characterized by extremely close interplanar distances and (ii) Ag nanocrystals. Moreover, the relative amount of the Ag crystalline phase in the samples corresponds to the ratio Ag/Fe during synthesis. Different shapes and sizes of NPs were observed in the TEM and HRTEM images. Ellipses,

quadrangles and hexagons with rounded corners with the characteristic sizes of 20–40 nm were the main types. Based on the literature data, the ellipse shaped NPs were attributed to both the Fe_3O_4 and the γ-Fe_2O_3 phases and quadrangle shaped NPs were ascribed to the Fe_3O_4 phase. The carbon shells of 1–3 nm in thickness were seen only in the HRTEM images (figures 2(b) and (e)). The shells were significantly thinner compared to the carbon shell thickness in the sample fabricated earlier at 395 °C. Approximately twice smaller spherical, completely opaque NPs with a size of 5–15 nm (sometimes larger) were determined as Ag nanocrystals. Ag NPs were located very close to the iron oxide NPs which suggested the formation of hybrid NPs Fe_xO_y@C-Ag. This assumption is well consistent with the observed decrease in the saturation magnetization of NPs with the increasing Ag concentration in the samples. Mössbauer spectra analysis showed that all the powdered samples synthesized at 370 °C except for sample 9 contain both magnetic phases Fe_3O_4 and γ-Fe_2O_3. The relative concentrations of these phases vary from sample to sample, but no regular connection with Ag concentration can be traced. Sample 9 contains only the γ-Fe_2O_3 phase.

MCD spectra were obtained for the first time both for the series of Fe_xO_y@C NPs synthesized at different temperatures from 360 to 400 °C and for Fe_xO_y@C NPs synthesized at 370 °C and modified with Ag. An excellent agreement is observed between the MCD spectra shape and sample phase composition obtained with the Mössbauer spectra. The MCD spectrum of sample 9 totally coincides with the γ-Fe_2O_3 MCD spectrum known in literature. For all other samples, two wide peaks of opposite signs characteristic of Fe_3O_4 are the prevailing features in the MCD spectra. They were ascribed by several authors to the interband electron transitions in magnetite. Distortion is noticeable on the high-energy slope of the positive peak due to the γ-Fe_2O_3 contribution. This contribution intensity correlates with the content of the γ-Fe_2O_3 phase in accordance with the Mössbauer data. An increase of the Ag content in the samples leads to the shift of the spectra to lower energies, approximately linear with the change of Ag concentration. Two different explanations of the shift origin are considered. The shift can be explained by the proximity of Ag and Fe_3O_4 NPs and the growing energy of the occupied and partly occupied bands under the influence of Ag. On the other hand, a possibility is considered of the contribution of the MCD related to the excitation of surface plasmon resonance in the Ag NPs into the observed MCD spectrum. The choice between these mechanisms requires additional experiments.

Acknowledgments

The reported study was funded by Joint Research Project of Russian Foundation for Basic Research № 19-52-52002 and Ministry of Science and Technology, Taiwan MOST № 108-2923-M-153-001-MY3 and № 106-2112-M-153-001-MY3. The samples of series 1 were studied with the support of the Ministry of Science and Higher Education of the Russian Federation within the State assignment FSRC «Crystallography and Photonics» RAS. The electron microscopy investigations were conducted in the SFU Joint Scientific Center supported by the State assignment (#FSRZ-2020-0011) of the Ministry of Science and Higher Education of the Russian Federation.

ORCID iDs

D A Petrov https://orcid.org/0000-0001-7228-2471
C -R Lin https://orcid.org/0000-0003-4880-6196
I S Edelman https://orcid.org/0000-0002-5589-6559
A O Baskakov https://orcid.org/0000-0002-5868-6354
S S Starchikov https://orcid.org/0000-0002-3201-4269

References

[1] Verwey E J W and Heilmann E L 1947 Physical properties and cation arrangement of oxides with spinel structures I. cation arrangement in spinels *J. Chem. Phys.* **15** 174–80
[2] Gao Q, Chen F, Zhang J, Hong G, Ni J, Wei X and Wang D 2009 The study of novel Fe_3O_4@ γ -Fe_2O_3core/shell nanomaterials with improved properties *J. Magn. Magn. Mater.* **321** 1052–7
[3] Hwang Y, Angappane S, Park J, An K, Hyeon T and Park J-G 2012 Exchange bias behavior of monodisperse Fe_3O_4/g-Fe_2O_3core/shell nanoparticles *Curr. Appl Phys.* **12** 808–11
[4] Lee S-C, Fu C-M and Chang F-H 2013 Effects of core/shell structure on magnetic induction heating promotion in Fe_3O_4/γ-Fe_2O_3 magnetic nanoparticles for hyperthermia *Appl. Phys. Lett.* **103** 163104
[5] Obaidat I M, Nayek C, Manna K, Bhattacharjee G, Al-Omari I A and Gismelseed A 2017 Investigating exchange bias and coercivity in Fe_3O_4–γ-Fe_2O_3 core–shell nanoparticles of fixed core diameter and variable shell thicknesses *Nanomaterials* **7** 415
[6] Obaidat I M, Nayek C and Manna K Investigating the role of shell thickness and field cooling on saturation magnetization and its temperature dependence in Fe_3O_4/γ -Fe_2O_3 Core/Shell nanoparticles 2017 *Appl. Sci. Basel* **7** 1269
[7] Nayek C, Al-Akhras M-A, Narayanaswamy V, Khaleel A, Al-Omari I A, Rusydi A and Obaidat I M Role of shell thickness and applied field on the magnetic anisotropy and temperature dependence of coercivity in Fe_3O_4/-Fe_2O_3 core/shell nanoparticles 2019 *Mater. Express* **9** 123–32
[8] Ramirez-Nuñez A L, Jimenez-Garcia L F, Goya G F, Sanz B and Santoyo-Salazar J 2018 In vitro magnetic hyperthermia using polyphenol-coated Fe_3O_4@γFe_2O_3 nanoparticles from Cinnamomun verum and Vanilla planifolia: the concert of green synthesis and therapeutic possibilities *Nanotechnology* **29** 074001
[9] Xie W, Gu L, Sun X, Liu M, Li S, Wang Q, Liu D and He D 2016 Ferrocene derived core-shell structural Fe_3O_4@C nanospheres for superior lithium storage properties *Electrochim. Acta* **220** 107–13
[10] Wang Y, Guo X, Wang Z, Lü M, Wu B, Wang Y, Yan C, Yuan A and Yang H Controlled pyrolysis of MIL-88A to Fe_2O_3@C nanocomposites with varied morphologies and phases for advanced lithium storage 2017 *J. Mater. Chem.* A **5** 25562–73
[11] Yin L, Jun Gao Y, Jeon I, Yang H, Kim J-P, Jeong S Y and Cho C R 2019 Rice-panicle-like γ-Fe_2O_3@C nanofibers as high-rate anodes for superior lithium-ion batteries *Chem. Eng. J.* **356** 60–68
[12] Wu G, Cheng Y, Ren Y, Wang Y, Wang Z and Wu H 2015 Synthesis and characterization of g-Fe_2O_3@C nanorod-carbon sphere composite and its application as microwave absorbing material *J. Alloys Compd.* **652** 346–50

[13] Sinana N and Unur E 2016 Fe_3O_4/carbon nanocomposite: investigation of capacitive & magnetic properties for supercapacitor applications *Mater. Chem. Phys.* **183** 571–9

[14] Lyubutin I S, Lin C-R, Tseng Y-T, Spivakov A, Baskakov A O, Starchikov S S, Funtov K O, Jhang C-J, Tsai Y-J and Hsu H-S 2019 Structural and magnetic evolution of Fe_xO_y@carbon core-shell nanoparticles synthesized by a one-step thermal pyrolysis *Mater. Charact.* **150** 213–9

[15] Xia H, Cui B, Zhou J, Zhang L, Zhang J, Guo X and Guo H Synthesis and characterization of Fe_3O_4@C@Ag nanocomposites and their antibacterial performance 2011 *Appl. Surf. Sci.* **257** 9397–402

[16] Liang H, Niu H, Li P, Tao Z, Mao C, Song J and Zhang S 2013 Multifunctional Fe_3O_4@C@Ag hybrid nanoparticles: aqueous solution preparation, characterization and photocatalytic activity *Mater. Res. Bull.* **48** 2415–9

[17] Zhu M, Wang C, Menga D and Diao G 2013 In situ synthesis of silver nanostructures on magnetic Fe_3O_4@C core–shell nanocomposites and their application in catalytic reduction reactions *J. Mater. Chem.* A **1** 2118–25

[18] Guo Y, Tang D, Zhang L, Li B, Iqbal A, Liu W and Qin W 2017 Synthesis of ultrathin carbon dots-coated iron oxide nanocubes decorated with silver nanoparticles and their excellent catalytic properties *Ceram. Int.* **43** 7311–20

[19] Li W H, Yue X P, Guo C S, Lv J P, Liu S S, Zhang Y and Xu J 2015 Synthesis and characterization of magnetically recyclable Ag nanoparticles immobilized on Fe_3O_4@C nanospheres with catalytic activity *Appl. Surf. Sci.* **335** 23–28

[20] Satvekar R K and Pawar S H Multienzymatic cholesterol nanobiosensor using core–shell nanoparticles incorporated silica nanocomposite 2018 *J. Med. Biol. Eng.* **38** 735–43

[21] An Q, Zhang P, Li J-M I, Ma W-F, Guo J, Hub J and Wang -C-C 2012 Silver-coated magnetite–carbon core–shell microspheres as substrate enhanced SERS probes for detection of trace persistent organic pollutants *Nanoscale* **4** 5210–6

[22] Ye Y, Chen J, Ding Q, Lin D, Dong R, Yang L and Liu J 2013 Sea-urchin-like Fe_3O_4@C@Ag particles: an efficient SERS substrate for detection of organic pollutants *Nanoscale* **5** 5887–95

[23] Chen J, Guo Z, Wang H-B, Gong M, Kong X-K, Xia P and Chen Q-W Multifunctional Fe_3O_4@C@Ag hybrid nanoparticles as dual modal imaging probes and near-infrared light-responsive drug delivery platform 2013 *Biomaterials* **34** 571–81

[24] Petrov D A *et al* 2020 Magnetic and magneto-optical properties of Fe_3O_4 nanoparticles modified with Ag *J. Magn. Magn. Mater.* **493** 165692

[25] Edelman I *et al* 2012 Magnetic nanoparticles formed in glasses co-doped with iron and larger radius elements *J. Phys. D: Appl. Phys.* **112** 084331

[26] Bruker AXS TOPAS 2008 *V4: General Profile and Structure Analysis Software for Powder Diffraction data—User's Manual* (Karlsruhe, Germany: Bruker AXS)

[27] Grau-Crespo R, Al-Baitai A Y, Saadoune I and De Leeuw N H 2010 Vacancy ordering and electronic structure of gamma-Fe_2O_3 (maghemite): a theoretical investigation *J. Phys.: Condens. Matter.* **22** 255401

[28] Powder Diffraction File (PDF 4+, 2020), Inorganic Phases Database, International Center for Diffraction Data (ICDD), Swarthmore, PA, USA. http://www.icdd.com/products/pdf4.htm

[29] Ruíz-Baltazar A, Reyes-López S Y, Esparza R, Estévez M, Hernández-Martínez Á, Rosas G and Pérez R 2015 Synthesis and characterization of bifunctional α-Fe_2O_3-Ag nanoparticles *Adv. Condens. Matter Phys.* **2015** 320873

[30] Wang R, Dang F, Liu C, Wang D-J, Cui P-X, Yan H-J and Zhou D-M 2019 Heteroaggregation and dissolution of silver nanoparticles by iron oxide colloids under environmentally relevant conditions *Environ. Sci.: Nano* **6** 195–206

[31] Veisi H, Mohammadi L, Hemmati S, Tamoradi T and Mohammadi P 2019 In situ immobilized silver nanoparticles on rubia tinctorum extract-coated ultrasmall iron oxide nanoparticles: an efficient nanocatalyst with magnetic recyclability for synthesis of propargylamines by A3 coupling reaction *ACS Omega* **4** 13991–4003

[32] Morales I, Costo R, Mille N, da Silva G B, Carrey J, Hernando A and de la Presa P 2018 High frequency hysteresis losses on γ-Fe_2O_3 and Fe_3O_4: susceptibility as a magnetic stamp for chain formation *Nanomaterials* **8** 970

[33] Khollam Y B, Dhage S R, Potdar H S, Deshpande S B, Bakare P P, Kulkarni S D and Date S K Microwave hydrothermal preparation of submicron-sized spherical magnetite (Fe_3O_4) powders 2002 *Mater. Lett.* **56** 571–7

[34] Zboril R, Mashlan M, Papaefthymiou V and Hadjipanayis G Thermal decomposition of $Fe_2(SO_4)_3$: demonstration of Fe_2O_3 polymorphism 2003 *J. Radioanal. Nucl. Chem.* **255** 413–7

[35] Smit J and Wijn H P J 1959 *Ferrites: Physical Properties of Ferromagnetic Oxides in Relation to Their Technical Applications* (Eindhoven: Philips' Technical Library)

[36] Singh P and Upadhyay C 2018 Role of silver nanoshells on structural and magnetic behavior of Fe_3O_4 anoparticles *J. Magn. Magn. Mater.* **458** 39–47

[37] Lin C-R, Tseng Y-T, Ovchinnikov S G, Ivantsov R D, Edelman I S, Fedorov A S, Kuzubov A A, Fedorov D A, Starchikov S S and Lyubutin I S 2014 Fe_3S_4 and Fe_3O_4 magnetic nanocrystals: magneto optical and Mössbauer spectroscopy study *Mater. Res. Express* **1** 025033

[38] Gehring G A, Alshammari M S, Score D S, Neal J R, Mochtari A and Fox A M Magneto-optic studies of magnetic oxides 2012 *J. Magn. Magn. Mater.* **324** 3422–6

[39] Neal J R, Behan A J, Mokhtari A, Ahmed M R, Blythe H J, Fox A M and Gehring G A Magneto-optical study of the Verwey transition in magnetite 2007 *J. Magn. Magn. Mater.* **310** e246–8

[40] Alshammari M S *et al* 2014 Magnetic properties of In_2O_3 containing Fe_3O_4 nanoparticles *Phys. Rev. B* **90** 144433

[41] Amendola V, Bakr O M and Stellacci F 2010 A study of the surface plasmon resonance of silver nanoparticles by the discrete dipole approximation method: effect of shape, size, structure, and assembly *Plasmonics* **5** 85–97

[42] Goncalves M R 2014 Plasmonic nanoparticles: fabrication, simulation and experiments *J. Phys. D: Appl. Phys.* **47** 213001

[43] Artemyev M, Krutokhvostov R, Melnikau D, Oleinikov V, Sukhanova A and Nabiev I 2012 Low-field magnetic circular dichroism in silver and gold colloidal nanoparticles of different sizes, shapes, and aggregation states *Proc. SPIE Plasmonics* **8457** 845729

[44] Shiratsu T and Yao H 2018 Size dependence of magneto-optical activity in silver nanoparticles with dimensions between 10 and 60 nm studied by MCD spectroscopy *Phys. Chem. Chem. Phys.* **20** 4269–76

[45] Hui P M and Stroud D 1987 Theory of Faraday rotation by dilute suspensions of small particles *Appl. Phys. Lett.* **50** 950–2

[46] Armelles G, Cebollada A, Garcia-Martin A and Gonzalez M U 2013 Magnetoplasmonics: combining magnetic and plasmonic functionalities *Adv. Opt. Mater.* **1** 10–35